tvst

Article

Quantitative Fundus Autofluorescence: Advanced Analysis Tools

Nikolai Kleefeldt[1], Katharina Bermond[1], Ioana-Sandra Tarau[1], Jost Hillenkamp[1], Andreas Berlin[1], Kenneth R. Sloan[2], and Thomas Ach[1]

[1] Department of Ophthalmology, University Hospital Würzburg, Würzburg, Germany
[2] Department of Computer Science, University of Alabama at Birmingham, Birmingham, AL, USA

Correspondence: Thomas Ach, Department of Ophthalmology, University Hospital Würzburg, Josef Schneider Strasse 11, 97080 Würzburg, Germany. e-mail: thomas.ach@ukbonn.de

Received: October 18, 2019
Accepted: May 18, 2020
Published: July 1, 2020

Keywords: quantitative fundus autofluorescence; image registration; standard retina; optical coherence tomography

Citation: Kleefeldt N, Bermond K, Tarau I-S, Hillenkamp J, Berlin A, Sloan KR, Ach T. Quantitative fundus autofluorescence: Advanced analysis tools. Trans Vis Sci Tech. 2020;9(8):2, https://doi.org/10.1167/tvst.9.8.2

Purpose: To use multimodal retinal images (including quantitative fundus autofluorescence [QAF]) for spectral-domain optical coherence tomography (SD-OCT)-based image registration and alignment. For each age decade of healthy adults, normative fine-grained QAF retinal maps are generated and advanced methods for QAF image analysis are applied.

Methods: Multimodal retinal images were obtained from 103 healthy subjects (age 19–77 years; unremarkable retina/macula, age-appropriate clear optic media). Custom written FIJI plugins enabled: (1) determination of the fovea in SD-OCT and the edge of the optic disc in infrared (IR) images; (2) alignment and superimposition of multimodal retinal images based on foveal and optic disc position; (3) plotting of normative QAF retinal maps for each decade; and (4) comparison of individual retinas with normative retinas of different decades using newly introduced analysis patterns (QAF97, freehand tool).

Results: SD-OCT based image registration enables easy image registration, alignment, and analysis of different modalities (QAF, IR, and SD-OCT here reported). In QAF, intensities significantly increase with age with two major inclines between the third/fourth and seventh/eighth decades. With aging, the parafoveal area of maximum QAF intensity slightly shifts from temporal-superior to temporal. Compared with standard QAF analysis, refined QAF analysis patterns reveal a more detailed analysis of QAF, especially in the diseased retina.

Conclusions: Age-related QAF normative retinal maps can be used to directly compare and classify individual's QAF intensities. Advanced QAF analysis tools will further help to interpret autofluorescence changes in normal aging and in the diseased retina in a multimodal imaging setting.

Translational Relevance: Advanced methods for QAF analysis link basic findings with clinical observations in normal aging and in the diseased macula.

Introduction

Retinal imaging has been extensively used for more than 100 years for in vivo imaging of the human retina and choroid. Currently, it is a hallmark in the diagnosis and therapy of retinal and macular diseases.

In 1995, several groups introduced in vivo fundus autofluorescence (FAF) imaging using scanning laser ophthalmoscopy[1] and spectrophotometry[2] techniques. The main source of FAF is the retinal pigment epithelium (RPE) due to its accumulation of autofluorescent granules, namely lipofuscin and melanolipofuscin.[3] The accumulation starts early in life, increases in normal aging, but decreases at higher age and in age-related macular degeneration (AMD).[4–8] In normals, lipofuscin and melanolipofuscin distribution shows characteristic regional differences in relation to the position of the fovea with an increasing number of lipofuscin granules at the perifovea and near-periphery.[5,9] These cellular and subcellular properties and variations of autofluorescent granule

distribution impact clinical FAF,[6] as described in numerous studies.[1,2,10,11]

For many years, a major limitation of FAF was its lack of quantification. In 2011, Delori et al.[12] introduced a clinical, although still experimental, imaging tool that enables quantification of FAF signal intensities. Briefly, the quantitative fundus autofluorescence (QAF) imaging device is a modified scanning laser ophthalmoscope with an internal standard reference. This standard reference is simultaneously excited during each FAF image acquisition and the FAF images can then be normalized to the standard reference signal, independent of camera and image acquisition settings.[13] Since then, QAF has been performed in studies with healthy[14,15] and diseased eyes, such as in AMD, hereditary retino-/maculopathies,[16–21] and inflammatory diseases.[22]

The analysis of QAF fundus images, however, still remains fragmentary because only a small area of the posterior pole is used for analysis. The device's internal software uses a pattern of 25 segments consisting of three concentric rings centered on the fovea with the edge of the outermost ring at the edge of the optic disc (referred to "original QAF grid" throughout the manuscript).[15] The placement of this pattern is solely based on the examiner's visual decision of the presumed correct position of the fovea and the optic disc. Furthermore, most of the earlier mentioned studies reported the mean QAF8 signal (mean of pixel intensities of the middle ring located at the perifovea, consisting of eight evenly spaced segments). These mean QAF8 values have been used to build up normative databases from healthy subjects[15] and to classify QAF intensities in diseased eyes, especially in AMD.[16,23] However, in AMD eyes, analysis using the mean QAF8 value is problematic because autofluorescence signals from small areas of pathology (e.g.,drusen or tiny areas of atrophy) vanish if the affected area covers only a small number of pixels. These few pixels might not significantly impact the overall mean QAF8 signal within a segment or the whole original QAF grid.

In addition, for proper description of physiological and pathological findings, tools for direct comparison of QAF images to other retinal imaging modalities would be desirable because different modalities highlight various retinal structures and could combine and enhance the advantages of multimodal imaging.

The aim of this study was to use multimodal retinal images (including QAF) for SD-OCT-based coregistration and alignment to create image stacks for each subject and normative standard QAF retinas of healthy adults for each age decade. Furthermore, the introduction of advanced tools for QAF image analysis will serve as a basis for the analysis of the diseased macula and retina.

Materials and Methods

The local ethics committee (University Würzburg) approved this study (approval #134/16) and all procedures adhered to the tenets of the Declaration of Helsinki. Before study inclusion, informed consent was obtained from the subjects after explanation of the nature and possible consequences of the study.

Healthy subjects (range, age 19–77 years) were consecutively recruited from the Department of Ophthalmology, University Hospital Würzburg, between September 2016 and April 2019 for multimodal imaging (Table 1). Inclusion criteria were being phakic and having clear lens with no signs of cortical or nuclear lens opacities. Exclusion criteria were previous intraocular surgeries or any history of corneal, retinal, or macular disease of the examined eye. Ophthalmologic assessments included best corrected visual acuity using Early Treatment Diabetic Retinopathy Study (ETDRS) charts, measurement of corneal curvatures (Zeiss IOL Master; Zeiss, Oberkochen, Germany), applanation tonometry, biomicroscopy of the anterior segment, and dilated indirect funduscopy (using 0.5% tropicamide, 2.5% phenylephrine for pupil dilatation).

For analysis and normative standard retinas, only subjects with normal ophthalmologic status, best corrected visual acuity $\geq$20/25, and age-appropriate clear optic media (cornea, lens, vitreous body) were included. Based on age, subjects were further distributed in decades.

Image Acquisition

Multimodal imaging included QAF, infrared (IR), and spectral-domain optical coherence tomography (SD-OCT; 6-mm horizontal macular scan, 35 frames, 49 B-scans, 20° x 20° field) using Spectralis and modified HRA2 (both Heidelberg Engineering, Heidelberg, Germany). All Spectralis and HRA2 images were adjusted using subject's individual corneal c-curves for proper image calculation.

The specifications of the modified HRA2 device and QAF image acquisition requirements have been described elsewhere.[15] Briefly, the HRA2 device contains an internal reference, which is simultaneously excited and captured during QAF imaging (excitation 488 nm, emission 500–750 nm; image size: 30° x 30°, 768 x 768 pixels). This ensures that laser power and camera settings (i.e., sensitivity), which might differ

Table 1. Study Population

Decade	Number of Subjects	Age (mean)	Age (range)	Female	Male
Third	25	24.1	19–30	8	17
Fourth	17	35.0	31–40	6	11
Fifth	19	45.5	41–50	6	13
Sixth	18	57.1	52–60	6	12
Seventh	17	63.8	61–69	7	10
Eighth	7	73.6	71–77	3	4
Total	**103**			**36**	**67**

from examination to examination or subject to subject, can then be normalized to the internal reference. For adequate QAF imaging, photoreceptor bleaching for at least 20 seconds[12] was followed by registration of 12 single QAF frames. These frames were immediately checked for quality (criteria: homogeneous illumination of the posterior pole, image centered on the fovea), and, if necessary, low-quality frames were removed. The remaining image frames (at least nine frames) were used to create an average QAF image using the manufacturer´s software. Subjects were excluded from analysis if fewer than nine frames were useable. The variability between two QAF measurements (two measurements on one day with complete reposition of patient and camera) was tested in a subsequent study with five subjects from each age decade randomly picked for test–retest reliability. The mean difference between two QAF measurements was 7.9% (median 6.4%; range 0.05%–22.3%). The device was regularly calibrated to ensure consistent QAF measurements.

Image Analysis Using FIJI Plugins

All images were further processed using custom written FIJI plugins (FIJI Is Just; ImageJ 2.0.0-rc-69/1.52p) (www.fiji.sc).[24] The plugins are available on request. Figure 1 explains the workflow of image acquisition and SD-OCT-based registration and analysis using different tools. From each subject, the eye with the best QAF image quality (see earlier text) was included. If images from both eyes showed equal quality, the left eye was chosen. For better illustration, all images were plotted as left eyes.

OCT-Based Assembling of Multimodal Image Stacks

During SD-OCT scanning of the macula, an enface IR image was simultaneously captured. This IR image was used to register images from other modalities (e.g., QAF). The registration process (registration of an image modality against the IR enface image) was performed by specifying two landmarks clearly visible in both images and manually drawing a line between these two landmarks. In most cases, vascular bifurcations were used for this purpose (Fig. 1A). Images were then aligned to the IR enface image using a transformation limited to translation, rotation, and uniform scaling (Fig. 1B). Finally, images from one subject were superimposed to create an image stack of the different image modalities, equally sized and oriented (Fig. 1C).

Determination of Fovea and Edge of Optic Nerve Head

The location of the fovea and the edge of the optic nerve head were determined using the macula SD-OCT scan (fovea) and the corresponding IR enface image (optic nerve head). Within the OCT B-scan with the maximal foveal depression and the rise of the external limiting membrane, the exact position of the foveola was marked (Fig. 1D). This position was simultaneously transferred to the IR image, delivering x- (position within the B-scan) and y-coordinates (location of the appropriate B-scan within the SD-OCT volume scan) for the foveal position. Next, the edge of the optic nerve head, closest to the fovea, was marked manually. These two locations (fovea and edge of optic nerve head) specify a two-dimensional (2D) coordinate system, which forms the basis for all subsequent analyses (e.g., positioning of analysis grids; see later text).

Processing QAF Images and Build-Up of Standard Retinas

QAF images were post-processed and adjusted for the device-specific reference calibration factor (as provided by Heidelberg Engineering), as well as subject's age to compensate for the attenuation of the QAF signal by age-related media changes,[25] as previously described.[12,15] Finally, QAF images were

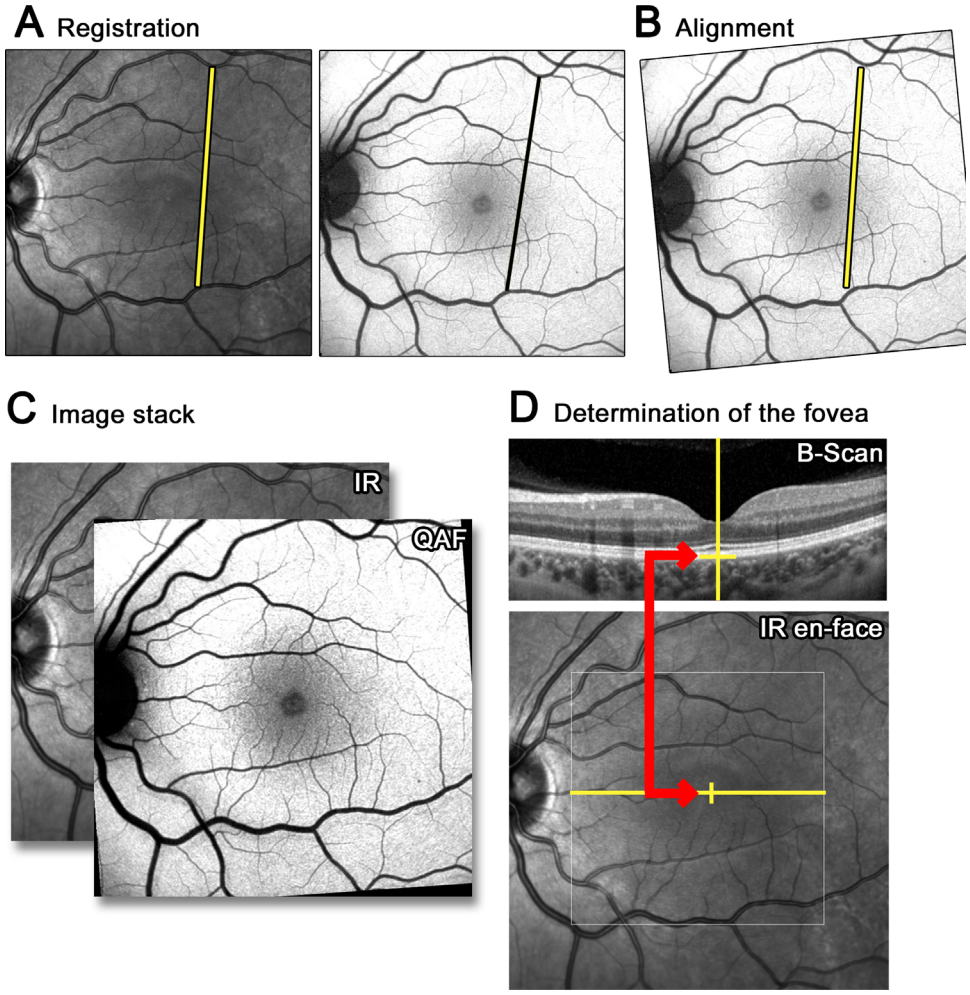

Figure 1. Workflow to create an image stack and determination of the fovea. (A) As a first step in the image registration process, a line connects two characteristic points (e.g., vessel bifurcations) within the localizer image (= simultaneously captured enface IR image during SD-OCT scanning) and the image to be registered (e.g., QAF image). (B) Adjustment of the registered image based on the two specified points by translating, rotating, and scaling of the image. (C) The registered images are grouped in a stack, aligned, and exactly superimposed. (D) The exact position of the fovea is determined within the SD-OCT scan showing the maximal foveal depression and the elevation of the external limiting membrane. The foveal position serves as a starting point for further image analysis (e.g., center of applied grids, see Fig. 2).

converted to colored 8-bit images, with QAF values limited to 0–511 and scaled to 0–255.

QAF data from subjects were combined to create normative standard retinal maps for each decade. Each standard retinal map maintains summary information (the sum and the sum of the squares) of the samples and the number of samples at each pixel in an image large enough to cover a field of view larger than the original QAF images. This allows the preparation of two standard maps showing: (1) the mean QAF value, and (2) the standard deviation of QAF values for each pixel at a given distance and orientation from the fovea.

With these normative standard retinas in the background, each newly QAF imaged retina can be compared with the appropriate (age-matched) QAF standard retinal map. In particular, it is possible to generate an image showing for each pixel (in the current QAF image) the deviation of that pixel from the mean within the age-matched standard retina, measured in units of the standard deviation from the mean observed at that location.

Application of Different Analysis Patterns

For the advanced analysis of QAF, several grids (ETDRS, original QAF grid,[15] newly introduced QAF97 pattern) were applied. All grids were centered on the fovea (as determined in the SD-OCT scans; see earlier text), with the optic disc on the negative x-axis (Fig. 2) and consists of different number of rings and subdividing segments. Although the EDTRS grid uses defined widths of its rings (1, 3, and 6-mm diameter), the original QAF grid and our extended

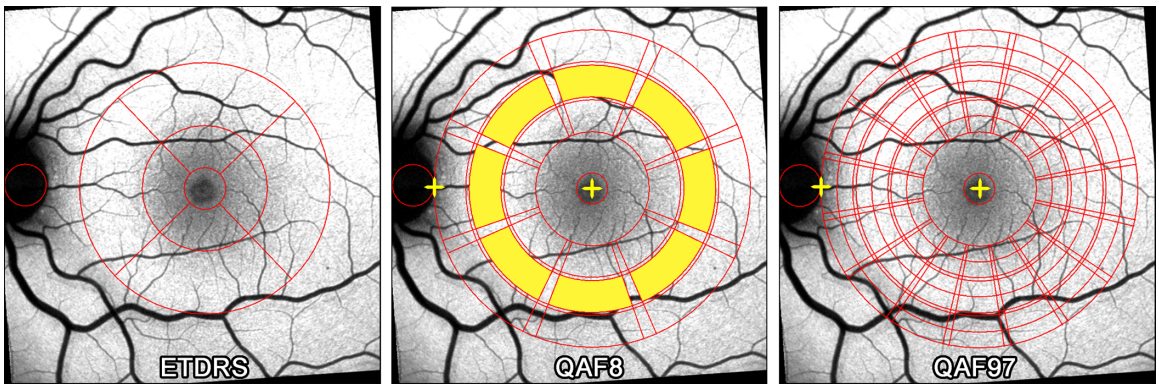

Figure 2. Different QAF analysis grids/patterns. The ETDRS pattern has a given, nonvariable size. For the original QAF grid (first described by Greenberg et al.[15] highlighted in yellow) and the newly introduced subsegmented QAF97 pattern, the distance between the center of the fovea and the edge of the optic nerve head is determined. Both patterns (QAF8, QAF97) are more variable in size compared with the ETDRS grid. The QAF97 grid is a modification of the originally introduced QAF pattern described by Greenberg et al.,[15] further subdividing each segment into four subsegments. Note: the red circle at the optic disc is just for illustration purposes but does not represent the actual size or dimensions of the optic nerve head.

QAF97 grid are based on the distance between the fovea and the edge of the optic disc, meaning that sizes of grid segments might slightly differ from eye to eye. The originally introduced grid by Greenberg et al.[15] contains three concentric rings, each with eight subdividing segments. Our QAF97 grid further bisects each original QAF ring segment (Greenberg et al.[15]), resulting in a total of 97 segments (Fig. 2).

For each segment (irrespective of the grid used), the mean, maximum and minimum values, standard deviation of QAF values, and the number of pixels of the analyzed area were written to a tab-delimited text file.

Freehand Analysis Tool

To enable detailed analysis of specific regions of interest, a polygon encircling conspicuous retinal areas can be drawn within one/multiple retinal image(s). Because all images from the different modalities are registered and aligned (see previous paragraphs), the exact position of the polygon can be transferred from one to any other modality. Thus a polygon may be drawn while viewing one modality (e.g., IR), and quantitatively analyzed using values from the QAF image. The freehand tool reports the mean intensity value, the standard deviation, the minimum and maximum values, and the number of pixels within the polygon. In this study, we typically report QAF values.

Statistics

Data collection, organization, and analysis were performed using Microsoft Excel 2016 (Microsoft Corporation, Redmond, WA) and SPSS statistic software package version 25.0 (IBM Corporation, Armonk, NY). Categorical variables are presented as numbers, and continuous variables are expressed as means ± standard deviation. A 1-way analysis of variance was conducted to assess age effects on QAF values measured with the different analyzing grids (QAF97, QAF8, and ETDRS). The post hoc analysis was performed using the Games-Howell test.

Results

Out of 123 initially imaged subjects, 103 subjects (Table 1) could be included in this study. All subjects were Caucasian. Twenty subjects had to be excluded due to low-image quality, lens status, or retinal abnormalities that could impact the QAF measurements. From all 103 subjects for final analysis, OCT-based registered and aligned multimodal image stacks were generated. Alignments were based on foveal position (as determined in the SD-OCT macula scan) and the edge of the optic nerve head (as determined in the IR image).

Advanced QAF Analysis

The introduction of an extended grid (QAF97) with a total of 97 segments (Fig. 2) enabled a more detailed analysis of the QAF intensities as compared with the commonly used original QAF grid segments. QAF97 covers the same area but has more segments, and therefore enables subtler analysis.

For all grids used (ETDRS, QAF8, QAF97), there was a significant increase in QAF intensity with aging ($P < 0.01$). QAF increases in all segments, including

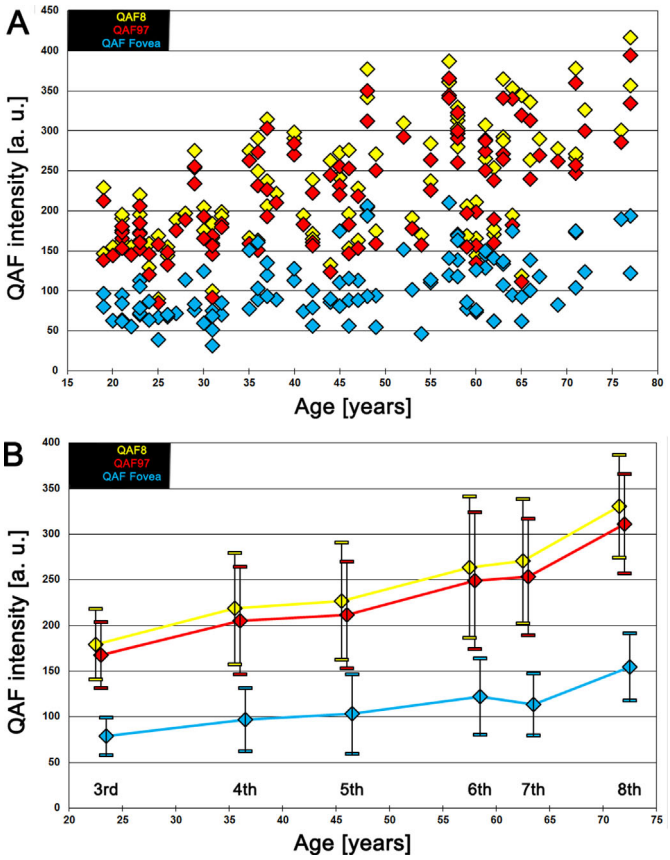

Figure 3. QAF8, QAF97, and QAF fovea. (A) QAF for each individual. (B). QAF for each decade. QAF increases with age, both at the perifovea/near periphery (QAF8, QAF97) and the fovea. However, extrafoveal QAF shows one slight plateau, between the fourth and fifth and between the sixth and seventh decades of age. Significant differences in QAF intensities were found between these decades: QAF97/QAF8: third–sixth, seventh, eighth; fourth–eighth; and fifth–eighth; QAF fovea: third–fifth, sixth, seventh, eighth; fourth–eighth; and fifth–eighth (for *P* values, see Supplementary Table S2). Presented are mean QAF values ± standard deviation. For each decade, QAF values for the median age within this age group is reported. Individual QAF values are summarized in Supplementary Table S1. a.u., arbitrary unit.

the fovea, with the exception of a small dip of QAF intensity at the fovea in decade 60 (Fig. 3, Supplementary Table S1). Interestingly, despite the continuing increase in QAF with age, between the fourth and fifth and between the sixth and seventh decades of age increase seems to slow down leading to the formation of a plateau (Fig. 3B).

QAF Normative Standard Retinal Maps

From all individuals in an age decade, the QAF images were aligned and superimposed to plot standard retinal maps (Fig. 4A). These standard retinal maps visualize the increase of FAF at the posterior pole with age, with highest FAF signals at the temporal/temporal-superior parafoveal region. FAF signal at the fovea is low and remains at low levels, although slightly increasing with aging. QAF values between age decades differ significantly ($P < 0.01$), irrespective of analysis grid used.

Interestingly, when considering the pixels with the highest QAF intensities in each of the six standard retinas, there is a noticeable shift of the hotspot with increasing age: from temporal-superior to temporal (Figs. 4B, 4C). This relocation starts in the 40s, with close approach of the horizontal line with higher age. Figure 4C plots the five segments with the highest QAF intensities, both using the original QAF grid (QAF8)[15] and the QAF97 grids. The QAF97 analysis presents a more detailed presentation of this hotspot migration.

Segment Subanalysis and Freehand Tool

The advantage of using a finer grid with smaller segments is demonstrated in Figure 5 and Supplementary Figure S1. Figure 5 shows an eye with geographic atrophy in non-neovascular AMD during a 9-month follow-up, with an enlargement of the geographic atrophy area. Using QAF8, QAF values (Table 2) from some segments might disregard the altered autofluorescence signal from the transition zone due to large atrophic areas within the same segments (see highlighted segments no. 1–4 [orange] in Figs. 5A, 5B). QAF97 enables a more detailed analysis and also takes the transition zone much more into account (Figs. 5C, 5D). With QAF97, the increase of the atrophic area, as well as the migration of transition zone, can be observed in more detail, as supported by numbers (see highlighted segments no. 1–7 [yellow] in Figs. 5E, 5F; Table 2). In addition, a freehand tool enables the measurement of QAF values independently from predefined segments (Figs. 5G, 5H; Table 2). By manually drawing polygons to mark specific lesions in any of the available images of the image stack (not restricted to the QAF image), QAF values can then be plotted from the corresponding QAF image.

Supplementary Figure S1 shows a patient suffering from Stargardt disease. Focusing the analysis just on the middle ring of the original QAF grid (Supplementary Fig. S1A) would miss other important pathologies (e.g., atrophic area at the posterior pole or other areas of focal hyperautofluorescence at the perifovea). The use of a finer grid (QAF97, Supplementary Figs. S1B, S1C) and a freehand tool (Supplementary Figs. S1B, S1D) enables a more detailed analysis of these pathologic areas. The overall retinal QAF is considerably increased (Supplementary Fig. S1E) in this Stargardt patient, further underlined by the marked deviation

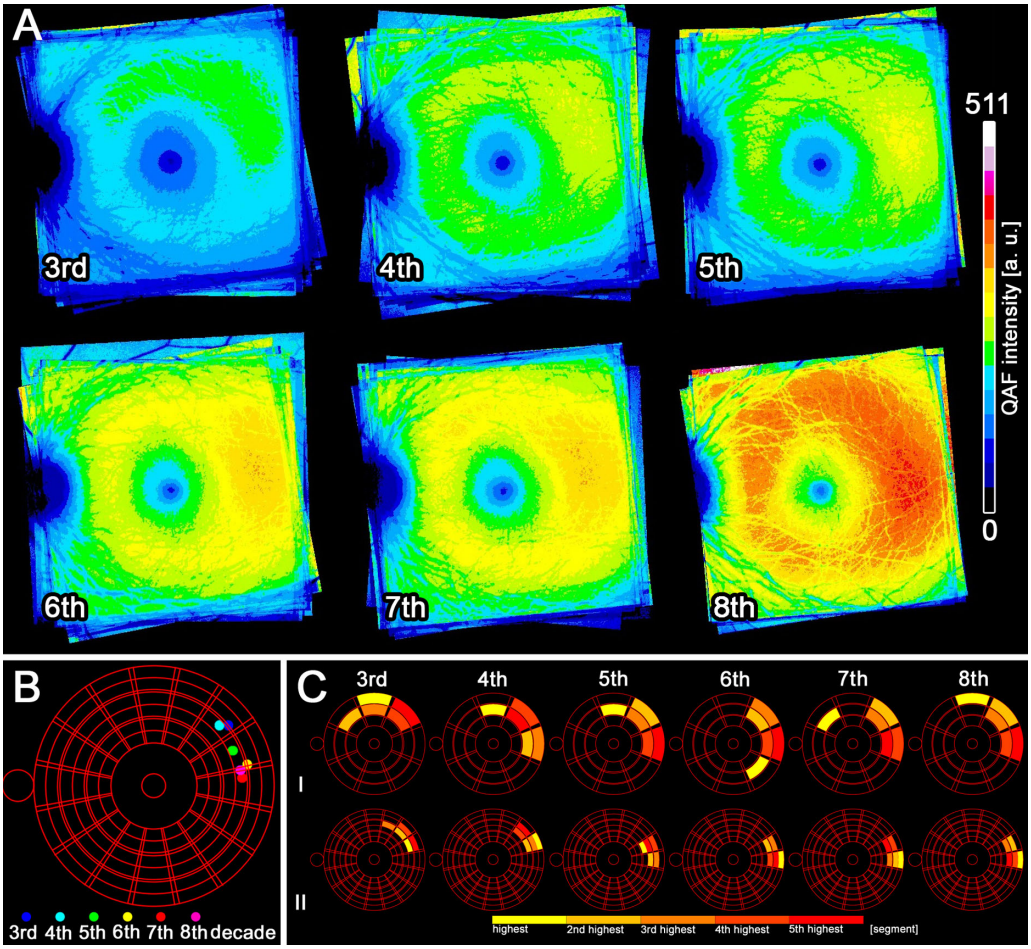

Figure 4. Color-coded QAF standard retinas for six decades and QAF hotspots. (A) By superimposing individual QAF images (aligned at the fovea and the edge of the optic nerve head), QAF standard retinas have been created for each decade (third–eighth decades). The QAF values of the standard retinas are color-coded and show a marked increase in intensity with increasing age, especially at the perifoveal region. (B) For each standard retina of the six decades, the pixel with the highest QAF value was determined and plotted on the QAF97 grid. With increasing age, there is a migration of the hotspot from temporal-superior to temporal. (C) Analysis of the highest segments of the original QAF and the QAF97 grids for the six decades. The segments with the five highest QAF values for each decade were marked in graded color (red = segment with the highest QAF intensity to yellow = segment with the fifth highest QAF intensity). The intervening segments are represented by orange tones. The five highest segments of the original QAF grid cover a much larger area of the retina and are mostly located in the temporal and superior retinal area. The five highest segments of the QAF97 cover a smaller retinal area and are limited to the temporal-superior and temporal retinal area. a.u., arbitrary unit.

from the normal QAF from an age-matched healthy control group (Supplementary Fig. S1F).

Although the original QAF grid (Fig. 5A, Supplementary Fig. S1A) and QAF97 (Fig. 5C, Supplementary Fig. S1B) cover the same area, the subsegmentation enables more detailed analyses, especially in pathologic findings that affect only small areas.

Discussion

Multimodal imaging of the human retina has become a standard procedure in the diagnosis and therapy control of retinal diseases. One of these techniques, FAF, reflects health and disease of the human outer retina, especially of the RPE. QAF, a recent further development in FAF imaging, surpasses an important limitation in FAF imaging: it enables comparisons of autofluorescence intensities among individuals and in the long-term follow-up by using an internal reference. In this study, we present QAF normative standard retinas for different age decades and advanced tools, which enable a detailed analysis of the QAF signal.

Our standard retinas demonstrate an increase of FAF with age, as previously reported.[12,15,26] Interestingly, increase in FAF between ages 20 and 70

Table 2. QAF Intensities ± Standard Deviation for a Subset of Segments Using the Original QAF8, QAF97, and the Freehand Tool in an Example of Geographic Atrophy (see Fig. 5)

Segment	Baseline QAF Value (a.u.)	Follow-Up (9 Months) QAF Value (a.u.)
QAF 8	160.6 ± 71.2	224.6 ± 38.2
Orange 1	254.2 ± 51.7	248.8 ± 53.8
Orange 2	92.7 ± 68.0	86.2 ± 58.9
Orange 3	93.2 ± 62.6	80.6 ± 53.4
Orange 4	173.5 ± 62.0	154.8 ± 59.4
Yellow 1	200.0 ± 76.6	194.2 ± 86.6
Yellow 2	218.1 ± 60.1	216.8 ± 75.4
Yellow 3	107.1 ± 69.4	95.3 ± 54.1
Yellow 4	127.3 ± 77.8	113.3 ± 74.4
Yellow 5	136.0 ± 65.0	119.5 ± 66.3
Yellow 6	158.9 ± 73.1	127.3 ± 71.6
Yellow 7	165.2 ± 36.7	154.4 ± 38.8
Freehand tool	163.8 ± 39.6	147.0 ± 51.1

a.u., arbitrary units.

years seems not to be linear. In fact, our data include a plateau mainly between the fourth and fifth and between the sixth and seventh decades of age, in which FAF shows no remarkable increase, whereas after age 60 years the autofluorescence intensities steeply raise. Similar findings were reported earlier from histological studies examining human donor eyes. Wing et al.[5] found a sigmoidal increase of RPE lipofuscin autofluorescence at the posterior pole, with greatest changes in the first two decades and then again after age 50 years. Feeney-Burns et al.[4] reported a marked increase of RPE lipofuscin granule load in the maturating eye (second decade), with a second steep increase after age 50 years.

Our classification using age decades is arbitrary; however, QAF standard retinas and the related standard deviation for each decade serve as a basis for direct comparisons of the QAF of individual subjects (with or without pathologies) with the associated age cohort. Such difference maps use the mean QAF values and the standard deviations that are specified for each pixel of the normative standard retina. These maps also reflect the distance of the QAF intensity to the standard retina in standard deviations pixel by pixel, and thus provide a valuable contribution to the detection of pathologies.

Highest FAF is normally found at the perifoveal region,[12,26] probably related to the specific photoreceptor distribution within this region (highest rod to cone ratio at the perifovea),[27] and subsequently the deposition of lipofuscin granules. A subanalysis of the standard retinas using the QAF97 grid revealed a migration of the QAF hot spots (highest points of QAF values) with increasing age, which is a new finding, and to the best of our knowledge not yet described. It remains unclear whether this is a biological or optical phenomenon of the aging eye.

QAF has been proven to be repeatable, reliable, and feasible for a standardized approach.[12,15,17] However, in QAF studies, QAF8 values are reported, which only cover a small area of the posterior pole[15] and ignore specific lesions outside this area. Also, reporting QAF8 values of pathologic findings requires a general involvement and altered FAF retinal signal, or at least a significant impact of the QAF8 area by pathologic lesions. In AMD, generally decreased QAF values have been shown[16,17] confirming findings from histology, which show rearrangement[8] and loss of RPE lipofuscin granules in AMD.[6,7] However, subtle changes or smaller lesions might be missed, which require advanced analysis grids or patterns. The herein described QAF97 and freehand tool enable a detailed analysis of pathologic lesions, such as the transition zone or atrophic areas in AMD.

Previous reports using the QAF8 pattern[17,20,28,29] reported one mean QAF8 value for one patient (whole eye assessment for population-based analysis), particularly to minimize variability. For our group of healthy subjects, a mean QAF8 variability of approximately 8% between two measurements can be considered good repeatability. The use of smaller subfields (QAF97) or freehand tool areas from a pathologic macula might increase the variability, as recently shown for pathologic eyes. In AMD, the variability is reported to be up to 20%.[17] Standardized imaging protocols, proper image acquisition, well-trained technicians, and

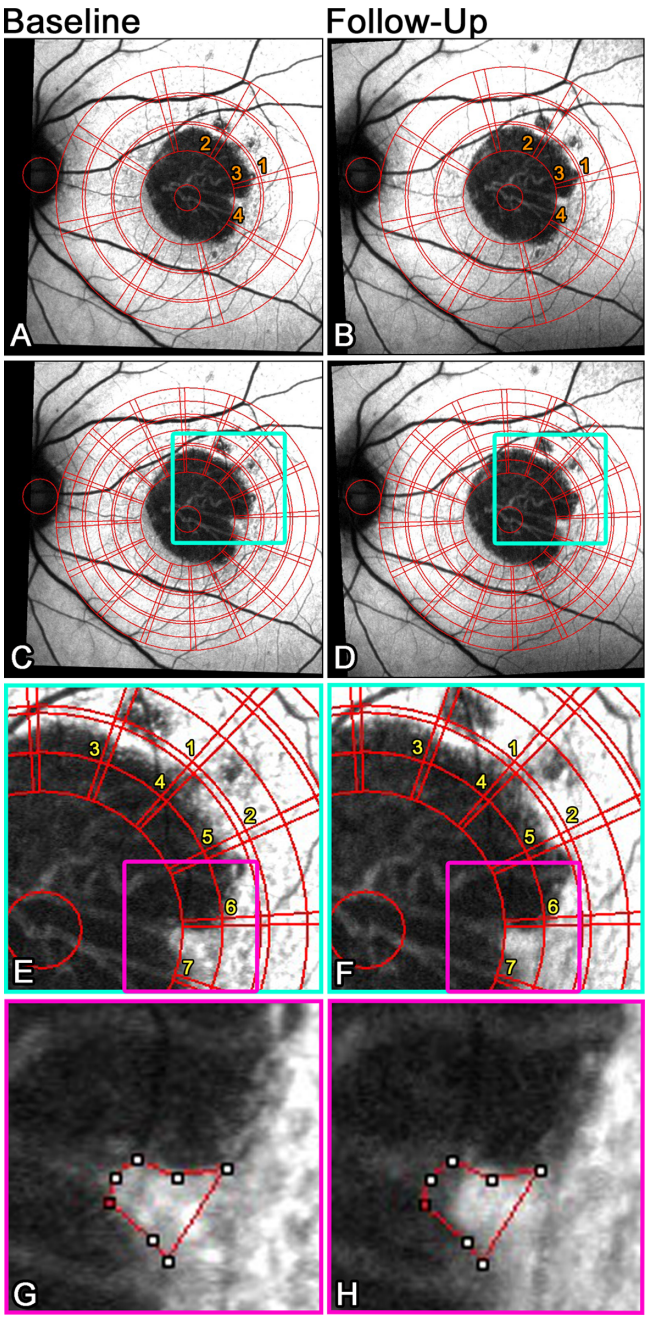

Figure 5. Comparison of original QAF grid, QAF97, and a freehand tool. An 87-year-old (pseudophakic) male patient with geographic atrophy at baseline and at 9 months follow-up, showing an enlargement of the atrophic zone. Using the QAF8 segments (A, B), the growth of the geographic atrophy/changes in transition zone might be missed because the segment area is too large to capture the growth effect. With the QAF97 grid (C–F), a finer analysis of the geographic atrophy/transition zone is possible. The freehand tool (G, H) enables analysis of conspicuous retinal areas. Different areas (transition or atrophic zones) can be analyzed individually (for QAF values, see Table 2). Note: the red circle at the optic disc is just for illustration purposes but does not represent the actual size or dimensions of the optic nerve head.

immediate image quality check could reduce QAF variability, although some uncertainty might remain.

To correlate QAF data with findings from other image modalities and/or devices, proper registration of all images is an indispensable prerequisite. Several methods for retinal image registration have been described, for example, by automated detection of retinal bifurcations,[30] the angle between these vessels,[31] and a Hough transform,[32] whereas others authors used an automatic retinal vessel detection to create vascular structure graphs, followed by graph matching of corresponding retinal images.[33] Spherical representation of the eye and registration in a three-dimensional (3D) model[34,35] are further options. Our registration methods are based on a manual selection of control points[36] and lead to image stacks with images of different modalities. Although the focus in this study was on QAF, this platform of registered image stacks will be the basis for future studies examining retinal and macular diseases. In addition, the SD-OCT-based application of foveal centered analysis grids will guaranty precise measurements and correlations along the image stack and along different imaging modalities, as well as in follow-ups.

We developed an SD-OCT/corresponding IR image-based approach to enable image registration and alignment. A requirement for standardized analysis is a common starting point. For this purpose, we chose the fovea and the edge of the optic disc, which could easily and repeatedly be determined using an SD-OCT scan (fovea) and the corresponding IR image (edge of the optic disc head). An image stack comprising all acquired images was assembled before further image analysis. The advantage of such an image stack is the potential of unlimited extension, meaning that new images from other modalities (e.g., color fundus photography, near-IR autofluorescence, or others) or from follow-up examinations can be uploaded at any time point to be registered against the basic IR image. Additionally, all modalities are registered to the full SD-OCT volume because all analysis plugins display the B-Scan stack and use cooperating cursors (x-y in the enface view, x-z in the B-Scan view) to facilitate 3D browsing. Future analysis tools can be applied to these image stacks, for example, registration of retinal vessels or calculation of macular pigment optical density, as explored in ongoing studies.

The limitation of such an SD-OCT-based method is the requirement of an OCT scan, which needs to come along with at least one simultaneously acquired fundus image. However, OCT devices often offer IR reflectance images for live image control. Macula wide SD-OCT scans that include the fovea (foveal pit, elevation of the external limiting membrane) and the optic

nerve head (Bruch membrane opening) could be used in future studies to further minimize subjective estimations. Further limitations of QAF imaging and its analysis are the dependence on clear optic media, in particular the lens. For our normative standard retinas, we only included patients with clear lenses (as revealed in slit-lamp biomicroscopy) and full visual acuity. However, it cannot be ruled out that subtle lens opacities impacted the total QAF values, especially in the elderly.

Conclusions

We present image registration tools to create QAF normative standard retinal maps, which can be used to easily compare with QAF from healthy or diseased individuals of the corresponding age group. Furthermore, we propose that the use of adjustable analysis tools might be a suitable way to analyze the diseased retina, as examined in ongoing studies.

Acknowledgments

Thomas Ach reports grants from the National Institutes of Health/National Eye Institute (1R01EY027948), grants from the Dr. Werner Jackstädt Foundation, and nonfinancial support from Heidelberg Engineering during the conduct of the study.

Parts of this article were presented at the International Spectralis Symposium, Bonn, Germany, October 2018, and the International Retinal Imaging Symposium, Los Angeles, California, USA, March 2019.

Disclosure: **N. Kleefeldt**, None; **K. Bermond**, None; **I.-S. Tarau**, None; **J. Hillenkamp**, None; **A. Berlin**, None; **K.R. Sloan**, MacRegen (I); **T. Ach**, Novartis (F, R), Roche (C), MacRegen (I)

References

1. von Ruckmann A, Fitzke FW, Bird AC. Distribution of fundus autofluorescence with a scanning laser ophthalmoscope. *Br J Ophthalmol*. 1995;79:407–412.
2. Delori FC, Dorey CK, Staurenghi G, Arend O, Goger DG, Weiter JJ. In vivo fluorescence of the ocular fundus exhibits retinal pigment epithelium lipofuscin characteristics. *Invest Ophthalmol Vis Sci*. 1995;36:718–729.
3. Feeney L. Lipofuscin and melanin of human retinal pigment epithelium. Fluorescence, enzyme cytochemical, and ultrastructural studies. *Invest Ophthalmol Vis Sci*. 1978;17:583–600.
4. Feeney-Burns L, Hilderbrand ES, Eldridge S. Aging human RPE: morphometric analysis of macular, equatorial, and peripheral cells. *Invest Ophthalmol Vis Sci*. 1984;25:195–200.
5. Wing GL, Blanchard GC, Weiter JJ. The topography and age relationship of lipofuscin concentration in the retinal pigment epithelium. *Invest Ophthalmol Vis Sci*. 1978;17:601–607.
6. Ach T, Huisingh C, McGwin G, Jr., et al. Quantitative autofluorescence and cell density maps of the human retinal pigment epithelium. *Invest Ophthalmol Vis Sci*. 2014;55:4832–4841.
7. Ach T, Tolstik E, Messinger JD, Zarubina AV, Heintzmann R, Curcio CA. Lipofuscin redistribution and loss accompanied by cytoskeletal stress in retinal pigment epithelium of eyes with age-related macular degeneration. *Invest Ophthalmol Vis Sci*. 2015;56:3242–3252.
8. Gambril JA, Sloan KR, Swain TA, et al. Quantifying retinal pigment epithelium dysmorphia and loss of histologic autofluorescence in age-related macular degeneration. *Invest Ophthalmol Vis Sci*. 2019;60:2481–2493.
9. Weiter JJ, Delori FC, Wing GL, Fitch KA. Retinal pigment epithelial lipofuscin and melanin and choroidal melanin in human eyes. *Invest Ophthalmol Vis Sci*. 1986;27:145–152.
10. Spaide RF. Fundus autofluorescence and age-related macular degeneration. *Ophthalmology*. 2003;110:392–399.
11. Schmitz-Valckenberg S, Holz FG, Bird AC, Spaide RF. Fundus autofluorescence imaging: review and perspectives. *Retina*. 2008;28:385–409.
12. Delori F, Greenberg JP, Woods RL, et al. Quantitative measurements of autofluorescence with the scanning laser ophthalmoscope. *Invest Ophthalmol Vis Sci*. 2011;52:9379–9390.
13. Armenti ST, Greenberg JP, Smith RT. Quantitative fundus autofluorescence for the evaluation of retinal diseases. *J Vis Exp*. 2016;109:53577.
14. Eandi CM, Nassisi M, Lavia C, Alovisi C, de Sanctis U. Macular pigment density and quantitative fundus autofluorescence in young healthy subjects. *Invest Ophthalmol Vis Sci*. 2017;58:2284–2290.
15. Greenberg JP, Duncker T, Woods RL, Smith RT, Sparrow JR, Delori FC. Quantitative fundus autofluorescence in healthy eyes. *Invest Ophthalmol Vis Sci*. 2013;54:5684–5693.

16. Gliem M, Muller PL, Finger RP, McGuinness MB, Holz FG, Charbel Issa P. Quantitative fundus autofluorescence in early and intermediate age-related macular degeneration. *JAMA Ophthalmol*. 2016;134:817–824.
17. Reiter GS, Told R, Baratsits M, et al. Repeatability and reliability of quantitative fundus autofluorescence imaging in patients with early and intermediate age-related macular degeneration. *Acta Ophthalmol*. 2019;97:e526–e532.
18. Burke TR, Duncker T, Woods RL, et al. Quantitative fundus autofluorescence in recessive Stargardt disease. *Invest Ophthalmol Vis Sci*. 2014;55:2841–2852.
19. Sparrow JR, Duncker T, Woods R, Delori FC. Quantitative fundus autofluorescence in best vitelliform macular dystrophy: RPE lipofuscin is not increased in non-lesion areas of retina. *Adv Exp Med Biol*. 2016;854:285–290.
20. Gliem M, Muller PL, Birtel J, et al. Quantitative fundus autofluorescence in pseudoxanthoma elasticum. *Invest Ophthalmol Vis Sci*. 2017;58:6159–6165.
21. Duncker T, Tsang SH, Woods RL, et al. Quantitative fundus autofluorescence and optical coherence tomography in PRPH2/RDS- and ABCA4-associated disease exhibiting phenotypic overlap. *Invest Ophthalmol Vis Sci*. 2015;56:3159–3170.
22. Boudreault KA, Schuerch K, Zhao J, et al. Quantitative autofluorescence intensities in acute zonal occult outer retinopathy vs healthy eyes. *JAMA Ophthalmol*. 2017;135:1330–1338.
23. Reiter GS, Told R, Baumann L, Sacu S, Schmidt-Erfurth U, Pollreisz A. Investigating a growth prediction model in advanced age-related macular degeneration with solitary geographic atrophy using quantitative autofluorescence. *Retina*. 2019; Oct 1. doi:10.1097/IAE.0000000000002653. Online ahead of print.
24. Schindelin J, Arganda-Carreras I, Frise E, et al. Fiji: an open-source platform for biological-image analysis. *Nat Methods*. 2012;9:676–682.
25. van de Kraats J, van Norren D. Optical density of the aging human ocular media in the visible and the UV. *J Opt Soc Am A*. 2007;24:58–88.
26. FoC Delori, DG Goger, Dorey CK. Age-related accumulation and spatial distribution of lipofuscin in RPE of normal subjects. *Invest Ophthalmol Vis Sci*. 2001;42:1855–1866.
27. Curcio CA, Sloan KR, Kalina RE, Hendrickson AE. Human photoreceptor topography. *J Comp Neurol*. 1990;292:497–523.
28. Reiter GS, Told R, Schlanitz FG, et al. Impact of drusen volume on quantitative fundus autofluorescence in early and intermediate age-related macular degeneration. *Invest Ophthalmol Vis Sci*. 2019;60:1937–1942.
29. Müller PL, Gliem M, Mangold E, et al. Monoallelic ABCA4 mutations appear insufficient to cause retinopathy: a quantitative autofluorescence study. *Invest Ophthalmol Vis Sci*. 2015;56:8179–8186.
30. Chaudrhy R-A, Klein J-C, Parra-Denis E. Ophthalmologic image registration based on shape-context: application to fundus autofluorescence (FAF) images. Proceedings of the 8th IASTED International Conference on visualization, imaging, and image processing, VIIP. 2008.
31. Laliberte F, Gagnon L, Sheng Y. Registration and fusion of retinal images–an evaluation study. *IEEE Trans Med Imaging*. 2003;22:661–673.
32. Zana F, Klein JC. A multimodal registration algorithm of eye fundus images using vessels detection and Hough transform. *IEEE Trans Med Imaging*. 1999;18:419–428.
33. Deng K, Tian J, Zheng J, Zhang X, Dai X, Xu M. Retinal fundus image registration via vascular structure graph matching. *Int J Biomed Imaging*. 2010;2010:1–13.
34. Lin Y, Medioni G. Retinal image registration from 2D to 3D. *2008 IEEE Conference on Computer Vision and Pattern Recognition, Anchorage, AK, 2008*. 2008;1–8.
35. Hernandez-Matas C, Zabulis X, Triantafyllou A, Anyfanti P, Argyros AA. Retinal image registration under the assumption of a spherical eye. *Comput Med Imaging Graph*. 2017;55:95–105.
36. Ryan N, Heneghan C, de Chazal P. Registration of digital retinal images using landmark correspondence by expectation maximization. *Image Vis Comput*. 2004;22:883–898.